Int J Adv Manuf Technol
DOI 10.1007/s00170-012-4029-z

ORIGINAL ARTICLE

An experimentally based thermo-kinetic phase transformation model for multi-pass laser heat treatment by using high power direct diode laser

Soundarapandian Santhanakrishnan · Fanrong Kong · Radovan Kovacevic

Received: 30 August 2010 / Accepted: 24 February 2012

Abstract Laser-based phase transformation hardening (LPTH), based on rapid heating and cooling cycles produces hard and wear-resistant layers only at the selective region of the components. However, the bulk mass of the material's core property is retained. The advantages of high power direct diode laser in comparison with other high power lasers (CO_2 and Nd:YAG) have put this type of laser as a main heat source for localized heat treatment. However, a tempered zone is formed in overlapping regions of a large heat-treated area during multi-pass laser heat treatment (MPLHT) that affects the uniformity of heat-treated depth of material. This study is focused on the development of a uniform hardness distribution model to minimize the tempering effect during the MPLHT process. A tool steel AISI S7 is heat treated by using different levels of laser power (1,400–1,800 W) and scanning speeds (15–25 mm/s). An experimentally based finite element (FE) thermal model is developed to predict the cross-sectional as well as surface temperature history of the MPLHT process. The temperature-dependent material properties and phase change kinetics are taken into account in the model. The laser beam is considered as a moving rectangular-shaped heat source (12 mm×1 mm) with a uniform distribution (top-hat) of laser power. The temperature history acquired from the FE thermal model is coupled with thermo-kinetic (TK) equations to determine the corresponding phase transformations and hardness. The tempering effect of MPLHT is studied for different sizes of overlap (1 mm–3 mm) and lengths of scan (10 mm–35 mm). The TK model results are verified with experimental ones to optimize the processing parameters. The optimized processing parameters, including laser power, scanning speed, size of overlap, and the length of scan are used to achieve a uniform hardness distribution and an even depth of heat treatment in the MPLHT area.

Keywords High power direct diode laser (HPDDL) · Laser-based phase transformation hardening (LPTH) · Multi-pass laser heat treatment (MPLHT) · Finite element (FE) model · Thermo-kinetic (TK) model

1 Introduction

In a number of industries, such as automotive, aerospace, and defense, wear-resistant, corrosion-resistant, and heat-resistant surfaces are needed to increase the components service life [1]. Laser-based phase transformation hardening (LPTH) is one of the emerging surface modification techniques has the advantage with respect to the traditional heat treatment processes to locally heat treat the selective region of components. LPTH, based on rapid heating and cooling cycles, produces hard and wear-resistant layers only at the selective regions exposed to the concentrated heat source; whereas, the bulk mass of the material's core property is retained. In LPTH, a high power moving laser beam locally heats up the surface of a metallic component (a narrow thin layer) to the austenite (γ) phase. Subsequently, the efficient conduction of heat to the surrounding bulk mass of the material (acting as a heat sink) induces the heated surface

S. Santhanakrishnan · F. Kong · R. Kovacevic
Research Center for Advanced Manufacturing,
Southern Methodist University,
Dallas, TX, USA

R. Kovacevic (✉)
Research Center for Advanced Manufacturing and Center
for Laser Aided Manufacturing, Southern Methodist University,
3101 Dyer Street,
Dallas, TX 75205, USA
e-mail: kovacevi@lyle.smu.edu

Published online: 25 March 2012

to quench very fast below the martensite starting (M_S) temperature, forming a martensite microstructure as a product of solid-state phase transformation. Therefore, the heat-treated metallic component's final hardness depends on the temperature–time-dependent phase changes and the changes in carbon solubility caused by solid-state phase transformations [2]. The iron-carbon phase diagram and the corresponding phase transformations of LPTH are shown in Fig. 1.

Nowadays, a high power direct diode laser (HPDDL) is successfully used in industry to locally heat treat the surface of metallic components to achieve the specified hardness with wear-resistant properties. In comparison to other high power lasers (CO_2, Nd:YAG), HPDDL has several advantages related to the localized heat treatment process. The focused HPDDL beam has a rectangular spot (12 mm × 1 mm) and a wavelength of 808 nm with better absorption by metals than in the case of CO_2 or Nd:YAG laser. A higher wall-plug efficiency (~30%) makes this type of laser more economical [3]. The entire unit is relatively small and compact so that it can be easily mounted on the robot arm. A more uniform distribution (top-hat) of laser power along the length of laser spot (12 mm) provides a more uniform depth of heat treatment. In addition, minimum distortion, a small heat-affected zone (HAZ), and a locally hardened zone are achieved [4].

A tool steel AISI S7 (0.53% *C*) is chosen for this study. This type of steel is a typical candidate material for a variety of cutting tools (dies and punches) involved in plastic deformation and sheet metal processes. The dies used in plastic deformation processes and punches and dies used in sheet metal processes require local heat treatment in order to withstand harsh working conditions [5]. When a larger surface area is heat treated, multiple scans by laser beam

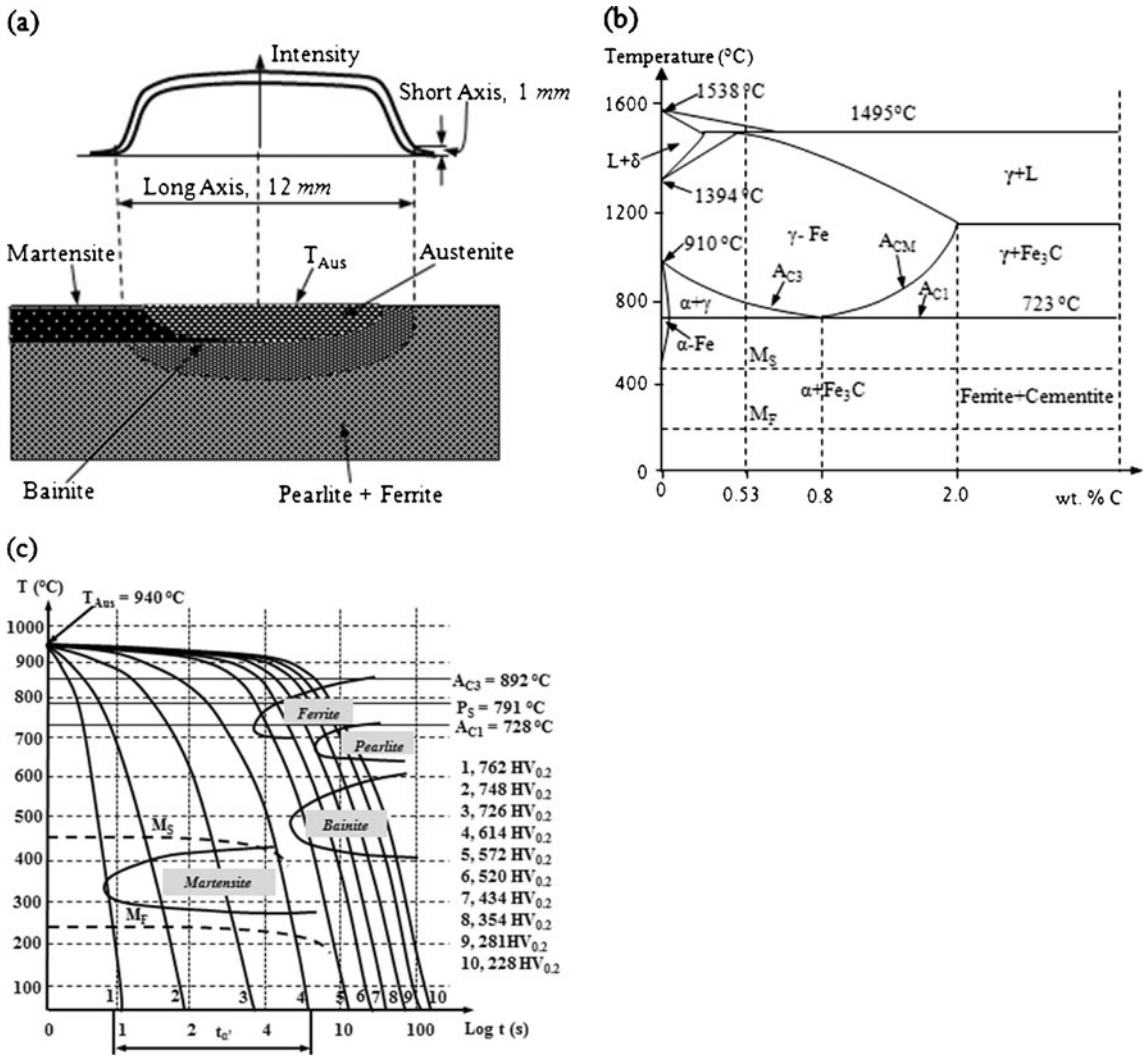

Fig. 1 **a** Physical mechanism of laser phase transformation hardening **b** combined with the iron-carbon phase diagram **c** CCT diagram for tool steel AISI S7 (0.53% C)

with slight overlaps are applied. Under this condition, the new heating cycle during the successive scan disturbs the normal cooling cycle of the heat-treated material that may generate a tempered microstructure. Based on the austenization starting (A_{C1}) and ending (A_{C3}) temperatures, three different conditions may occur during the heating cycle of multi-pass laser heat treatment (MPLHT) process: (1) if the material is heated more than A_{C3}, the material is fully austenized, and in the cooling cycle, it should be transformed into martensite; (2) for temperatures between A_{C1} and A_{C3}, a partial austenization is achieved; and (3) for a temperature less than A_{C1}, no austenization occurs [6].

As mentioned in literature [6–8], a range of tempered microstructure is generated when the material is tempered between 100°C and the A_{C1} temperatures. A precipitation of ε-carbide (Fe_2C) within the martensite is formed between the tempering temperatures of 100 to 200°C. In this temperature range (100 to 200°C), the martensite is still supersaturated with carbon; whereas, the martensite decomposition occurs at higher temperatures [8]. For a tempering temperature between 200°C and 350°C, the martensite decomposes into ferrite and cementite. A cementite (Fe_3C) precipitation within the martensite occurs between the tempering temperature of 350 and 500°C, whereas the tempering temperature between 500 and 700°C induces more precipitation of carbides within the martensite. Further, if the tempering temperature is above 700°C, the retained austenite is destabilized due to the precipitation of carbides. During this destabilization process, the austenite could release the internal stresses that transform the austenite partially or totally into martensite. This new structure is called tempered martensite [8]. The mentioned tempering effects could produce a non-uniform hardness distribution across the depth of heat treatment that could generate cracks [9].

In MPLHT, the majority of the studies focused on thermal modeling by means of analytical [10], or numerical solutions [9, 11–17] and experimental investigations [18]. Recently, several works [9–15] reported using the back tempering model [9, 11] to account for the effect of reaustenization [9, 10, 15–18] on the martensite–austenite phase changes [10, 11, 15–17] that occur during MPLHT. In order to reduce the tempering effect in the overlapped region, Fortunato et al. [15] proposed a simulator that is based on the tempering temperature and time to optimize the process parameters including laser power, scanning speed, overlapping ratio, and number of passes. The authors claimed that the model could predict the hardness distribution for the heat-treated surface for any given process parameters. Campana et al. [16] proposed a statistical method, named the covering uniformity (CU) index that is used to evaluate the efficiency of the MPLHT process. The index of CU is defined as a parameter that represents the process efficiency in terms of the percentage of effectively heat-treated area over the total heat-treated area. Based on the value of the CU index, the hardness uniformity of the heat-treated surface was evaluated with respect to a specific set of process parameters. In addition, the effect of the scanning path and overlapping ratio on the variation of hardness distribution across the depth of heat treatment for a given set of process parameters was also evaluated.

Bailey et al. [17] extended the work of Skvarenina et al. [14] to develop a 3-D phase transformation model to predict the temperature history, phase transformations, and hardness distribution for a laser heat treated cylindrically shaped geometrical part. In this model, an adjusted thermal conductivity and heat transfer coefficients were introduced to obtain the temperature distribution for the irregular complex-shaped regions. Rana et al. [18] performed a detailed experimental study for single pass and MPLHT to analyze the influence of the process parameters such as laser power, scanning speed, and laser spot size, and the carbon content (wt%) of the treated material with respect to the variation in microstructure, and hardness. The authors reported that the hardness improvement could be achieved by using an optimum scanning speed and laser spot size, while keeping the laser power constant. For MPLHT, they observed that a 30% overlapping ratio significantly reduces the tempering effect. If the overlapping ratio is larger than 30%, the tempering effect that greatly affect the hardness variation between the passes is more pronounced.

Yao et al. [10] developed an analytical model based on the principle of carbon diffusion and martensite decomposition at different levels of activation energy to study the tempering effect in the overlapped region for MPLHT. The authors reported that the tempering effect in the overlapped region is highly influenced by the carbon diffusion at various levels of activation energy and the cooling rate generated in the process. Moreover, the carbon atom diffusion in carbon and alloyed steels is easier than for other alloying elements due to its lower diffusion activation energy [8]. From this perspective, the tempering is a process controlled by the diffusion of carbon atoms. Capello et al. [19] developed an optimization model considering the depth of heat treatment and hardness as constraints to heat treat a maximum surface area under a minimum laser on time for a cylindrically shaped component. A three-level factorial design followed by a regression analysis was performed to obtain an optimal region of the processing parameters such as the scanning speed, overlapping ratio, and focal distance. This optimal combination of processing parameters was used to achieve the required depth and level of hardness while minimizing the tempering effect.

A fast and non-diffusion controlled phase transformation is generated during MPLHT [9, 10]. Therefore, the selection of process parameters to achieve the specified depth of heat treatment and hardness is considered to be a difficult task. Moreover, the industry is imposing the laser surface

treatment specifications in terms of the depth of heat treatment and magnitude of hardness. From this perspective, an experimentally based thermo-kinetic phase transformation model is a necessity in order to achieve a uniform hardness distribution and an even heat-treated depth during MPLHT. Foroozmehr and Kovacevic [6] developed a thermo-kinetic phase transformation model for the laser powder deposition (LPD) process to study the effect of deposition paths with respect to the change in hardness. Different deposition paths, such as long-path, short-path, spiral-in, and spiral-out were used to determine the temperature history, the presence of austenite, the level of martensite decomposition, and the final hardness of the LPD process. The authors found that the short path could produce a fairly uniform hardness. Therefore, a short continuous path with different lengths of scan is designed in this model to study the temperature history, phase transformations, and hardness of the MPLHT process. The idea is to maintain the temperature of the overlapped region in a multi-pass heat-treated area between the A_{C1} and A_{C3} temperatures by the heat accumulation from the successive scans of the laser beam. The heat accumulation from the previous scan could be used to minimize the tempering effect in the multi-pass heat-treated area [6–9]. Subsequently, a fairly uniform hardness distribution across the multi-pass heat-treated area is achieved.

In this study, an experimentally based finite element (FE) thermal model is developed for an MPLHT process to predict the thermal cycle for each point inside the workpiece. The FE thermal model results are coupled with thermo-kinetic equations to obtain the phase transformations and hardness of the MPLHT process. The phase transformation model can be used to determine the microstructure variations with respect to the sum of phase fractions and the corresponding phase hardness experienced by the material as a function of the thermal cycle. The thermal cycle generated during the MPLHT process is a function of process parameters such as the laser power and scanning speed, and the length of scan that can be used to predict the hardness and the depth of heat treatment. The numerical simulation results are verified with the experimental ones to obtain the optimum processing parameters. The optimum processing parameters are used to achieve a uniform hardness distribution across the depth of heat treatment.

2 Experimental setup and procedures

The base material used in this study is a tool steel AISI S7. Its chemical composition is summarized in Table 1. A flow chart with a coupon preparation prior to heat treatment and subsequent mechanical testing and microstructure characterization is shown in Fig. 2.

The coupon preparation prior to pre-heat treatment includes: (1) cutting the coupons with an abrasive water jet (AWJ) machine to a size of 50 mm × 35 mm × 10 mm, followed by (2) grinding the top surface of the coupon to remove the oxide layer. Stepwise grooves (3) are made through the bottom of the coupon up to a distance of 0.5 mm, 1 mm and 1.5 mm below the top surface of the coupon in which the thermocouples are placed. The coupons are sand-blasted (4) with aluminum oxide particles in a blasting chamber to increase the laser coupling efficiency by roughening the top surface of the coupon. The surface roughness of a base material is measured (5) by a roughness measuring instrument (Mitutoyo SJ-201). The coupon dimensions and its surface roughness measurement path are shown in Fig. 3. An average roughness (R_a) is recorded as 1.05 μm.

An advanced digital micro-hardness tester (Clark CM-700 AT) is used (6) to measure the base material hardness. A load of 200 gf for a dwelling time of 15 s is used for all the measurements. The base material hardness measurement locations are shown in Fig. 3. The measured value of the average surface hardness of the base material is 210 $HV_{0.2}$. Thermocouples are set (7) in the coupon's grooved locations and top surface (see Fig. 4c) along the center of the first pass, the center of the overlapped region, and the center of the second pass to obtain the cross-sectional as well as the surface temperature history. The coupon is clamped (8) in a specially designed fixture (see Fig. 4d). A three-level factorial of the design of experiments (DOE) is designed (9) in this work. The DOE and the process parameters levels are shown in Table 2.

A 2-kW direct diode laser of 808 nm in wavelength with a laser beam spot size of 12 mm × 1 mm (width × length) is used to heat treat the coupons of tool steel AISI S7. Laser power from 1,400 to 1,800 W at increments of 200 W and scanning speeds from 15 to 25 mm/s at intervals of 5 mm/s are used to carry out the experiments. The tempering effect of MPLHT is studied for different sizes of overlap (1–3 mm) and different lengths of scan (10–35 mm). The laser head is attached to a six-axis industrial robot. The whole experimental setup is shown in Fig. 4a. A chiller is used to cool the laser head, and argon shielding gas is used to prevent the material from oxidation at higher temperatures. The power control of the direct diode laser is integrated with a robot controller. Therefore, the laser power, scanning speed, and time delay between overlapping passes, and the length of scan can be controlled by a robot program.

Table 1 Chemical composition of tool steel AISI S7 [5]

Element	C	Mn	Si	Cr	Mo	V	Cu	P	S
Weight (%)	0.53	0.20–0.80	0.20–1.00	3.25	1.30–1.80	0.25	0.25	0.03	0.03

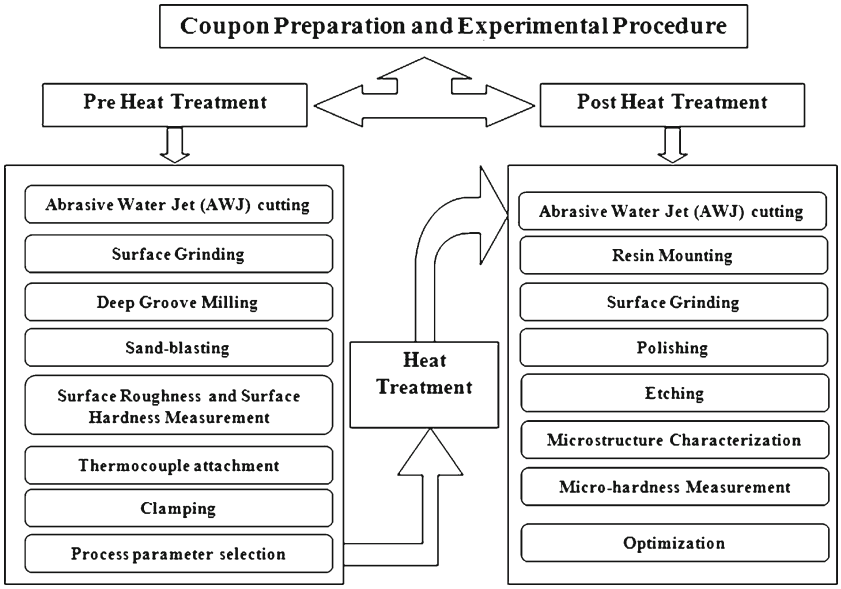

Fig. 2 Flow chart of experimental procedures including coupon preparation

The coupon preparation prior to post-heat treatment includes: (1) cutting the heat-treated coupons by an AWJ machine to a size of 30 mm×6 mm×10 mm; (2) mounting the coupons in a cylindrical enclosure of 50 mm in radius and 6 mm in height made of a polyvinyl chloride (PVC) thermoset filled up with 9:1 proportion of the mixture of resin (RR 128) and hardener (RH 16); (3) gradually grinding the top and bottom surfaces of the mounted coupons using a lower feed rate to remove the oxides and make the coupon surfaces flat; (4) polishing the coupons on the Mark V Lab 3B/4B dual wheel machine by using a different GRIT of 120, 240, 400, 600, 800, and 1,000 slicon carbide impedded papers in a plenty of water cleansing environment; (5) mirror polishing the coupons on the rotating velvet cloth disk by using an alumina powder paste of 1 μm and 0.05 μm; and (6) etching the coupons with 2% Nital followed by cleaning the coupons with alcohol for a standard metallographic procedure.

Etched coupons micrographs are taken by an ultra high-resolution optical microscope (Keyence VHX-500K). An

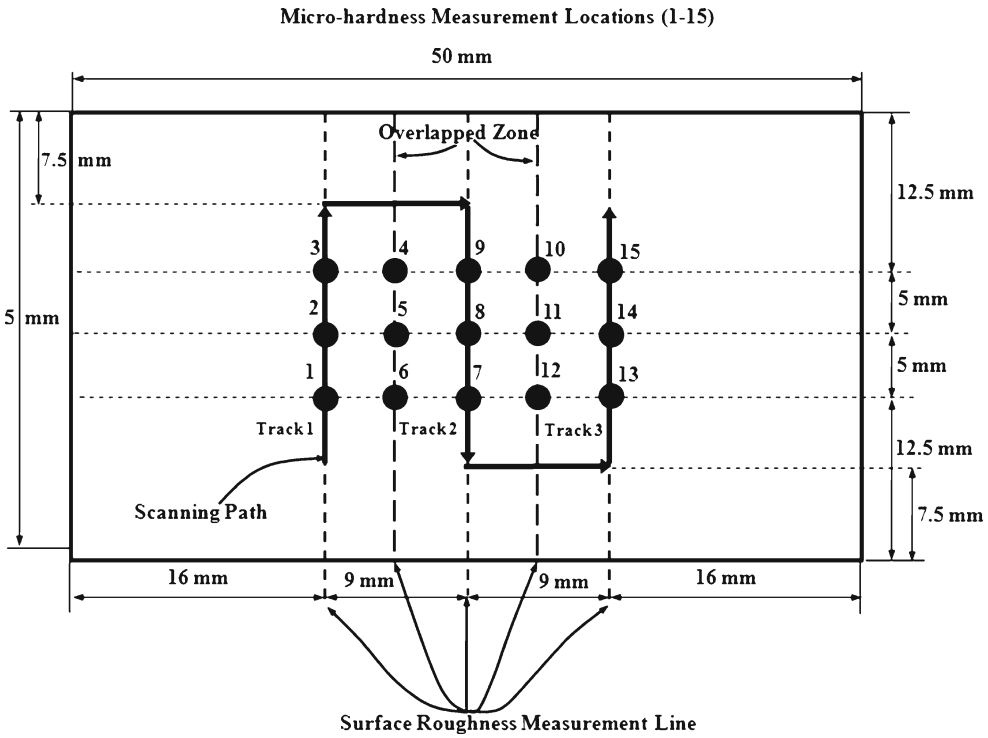

Fig. 3 Surface roughness measurement and micro-hardness measurement locations

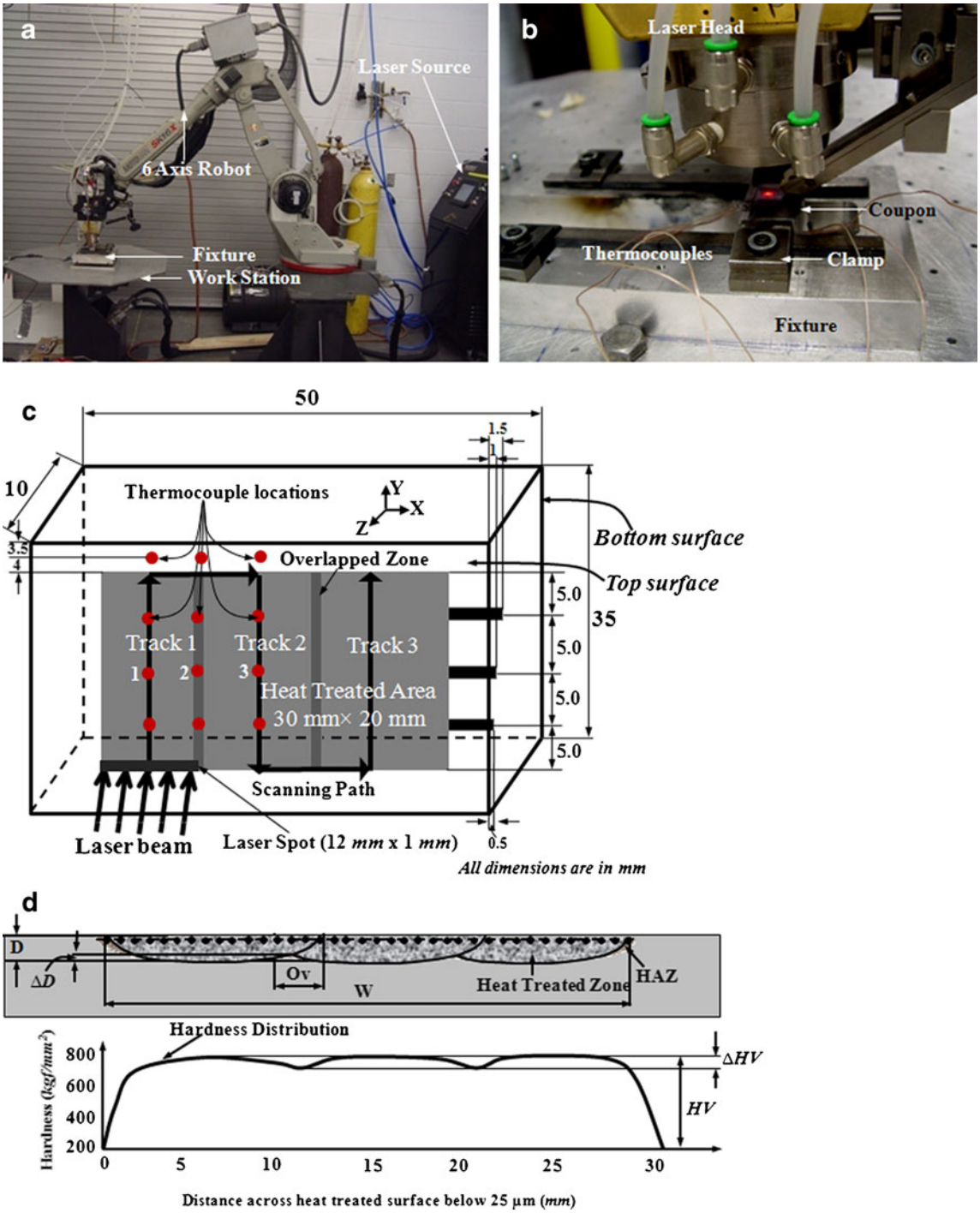

Fig. 4 Experimental setup for multi-pass laser heat treatment **a** complete system, **b** workstation, **c** schematic presentation of coupon dimensions and thermocouple locations **d** cross-section of multi-pass laser heat-treated zone with micro-hardness measurement data

optical micrograph at the magnification of ×50 in a bright field is used to measure the width of the heat mark (w) and depth of heat treatment (D) as shown in Fig. 4d. A scanning electron microscope (SEM) at a magnification of ×2,000 is used to characterize the microstructure of the heat-treated zone, the HAZ, and the base material. The cross-sectional micro-hardness of the heat-treated zone is measured by a digital micro-hardness tester (Clark CM-700 AT). A load of 200 gf and a dwelling time of 15 s is used to make an indentation on the measuring spot. The Vickers hardness is automatically calculated based on the image of the diagonal length of the resulting permanent indentation taken by the camera fixed above the measuring spot.

Table 2 Design of experiments and the levels of process parameters

Process parameters	Level 1	Level 2	Level 3	No of experiments
Laser power (W)	1,400	1,600	1,800	3
Scanning speed (mm/s)	15	20	25	3
Overlap (mm)	1	2	3	3
Total no of experiments				27

3 Finite element model

The laser heat treatment is a time-temperature and material-dependent process [2]. The temperature evolution across the coupon is dependent on the process parameters. The depth of heat treatment, the microstructure, and the corresponding hardness of the heat-treated area are dependent on the thermal cycle. A finite element method (FEM) is used to solve the heat conduction equation shown in Eq. 1. The ANSYS (11.0) software with APDL (ANSYS Parametric Design Language) is used to generate a numerical code to predict the temperature history of the heat-treated coupon for various process parameters [20].

3.1 Governing equation

In laser heat treatment, a high power density laser beam is irradiated at the top surface of the coupon to locally heat a thin layer of the substrate to the austenite temperature. When the laser moves to the next location, the self-quenching effect of the bulk mass of the material reduces the transformation temperature quickly to the M_S temperature. At the M_S temperature, the austenite phase is quickly transformed into the martensite phase. Therefore, a transient 3D heat conduction model is developed for the heat flow analysis that can predict the temperature distribution inside the coupon.

A 3D transient heat conduction governing equation for a homogeneous, isotropic solid material without heat generation in a rectangular coordinate system (x, y, z) is described below [21]:

$$\rho\frac{\partial(c(T)}{\partial t}=\frac{\partial}{\partial x}\left(\frac{\partial(k(T)}{\partial x}\right)+\frac{\partial}{\partial y}\left(\frac{\partial(k(T)}{\partial y}\right)+\frac{\partial}{\partial z}\left(\frac{\partial(k(T)}{\partial z}\right) \quad (1)$$

where, ρ is the density of material (in kilograms per cubic meter), $c(T)$ is the temperature-dependent specific heat (in joules per kilogram per degree Celsius), and $k(T)$ is the temperature-dependent thermal conductivity of the material (in watts per meter per degree Celsius).

In Eq. 1, the left-hand side describes the transient term, and the right-hand side describes the diffusion terms in 3D. In laser heat treatment, the temperature distribution inside the coupon across the x, y, and z direction is inhomogeneous. Therefore, a transient term and the diffusion terms are included in Eq. 1. The temperature-dependent material properties such as specific heat, $c(T)$, thermal conductivity, $k(T)$ and density, ρ are given in Table 3. In laser heat treatment, the thermal energy inside the coupon is generated by the absorption of laser radiation and subsequent heat conduction of the bulk mass of the material. There is no accumulated thermal energy inside the coupon. Therefore, no source term is included in the governing Eq. 1.

3.2 Coupon geometry

The heat-treated coupon's geometry, coordinate system (x, y, z), scanning direction (y-axes), and the boundary conditions are shown in Fig. 5. The x-axis refers to the direction along the length (L) of the coupon. The y-axis refers to the direction along the width (W) of the coupon and the scanning direction of the laser beam as well. The z-axis refers to the direction across the height (H) of the coupon. A rectangular-shaped laser spot (12 mm × 1 mm) of a uniform distribution (top-hat) of laser power is moving along the scanning direction (y-axes). This high power laser beam generates a constant heat flux ($\dot{q}$) that increases the temperature distribution across the cross-section (z-axes) of the coupon.

3.3 Boundary conditions

In FEM, the numerical simulation of temperature distribution of the heat-treated coupon governed by Eq. 1 is subjected to the following boundary conditions shown in Fig. 5. At time,

Table 3 Temperature-dependent thermal properties of tool steel AISI S7 [10]

Temperature (°C)	Specific heat (J/kg°C)	Thermal conductivity (W/m°C)	Density (kg/m^3)
25	460	28.9	7,760
100	473	30.8	7,740
200	485	32.7	7,721
300	496	34.6	7,703
400	512	38.5	7,680
500	529	42.3	7,636
600	541	46.2	7,612
700	556	50.2	7,590
800	579	53.9	7,552
900	594	57.7	7,268
1,000	619	59.5	7,218
1,100	635	17.5	7,055
1,200	664	23.4	6,757
1,300	691	26.3	6,715
1,400	718	28.5	5,902

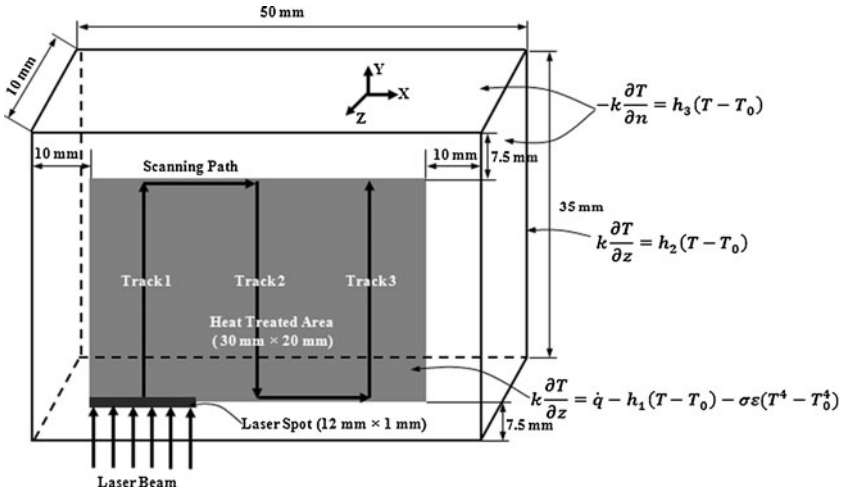

Fig. 5 Schematic presentation of coupon geometry, laser beam scanning direction and boundary conditions

t=0, the initial temperature of the coupon, T_0=25°C, and the initial state of the coupon are described below [21]:

$$T(x, y, z) = T_0 \tag{2}$$

Eq. 1 is subjected to boundary conditions (shown in Fig. 5) taking into account the heat introduced to the coupon by the laser beam. The heat dissipated by convection at the boundary surfaces and the heat radiated from the top surface of the coupon are described by Stefan–Boltzmann's law as given below [21]:

$$k\frac{\partial T}{\partial z} = \dot{q} - h_1(T - T_0) - \sigma\varepsilon\left(T^4 - T_0^4\right) \tag{3}$$

In Eq. 3, the term on the right-hand side representing the applying heat flux ($\dot{q}$) is perpendicular to the scanning direction of the laser beam, h_1 is the forced convection coefficient (in watts per square meter per degree Celsius) at the top surface, T is the surface temperature (in degrees Celsius) of the coupon, T_0 is the room temperature (in degrees Celsius), σ is the Stefan–Boltzmann constant (5.67×10^{-8} W/m^2 °C^4), and ε is emissivity (0.25) of the surface [21]. At the top surface of the coupon (x, y, 0), a part of the energy delivered by the laser radiation is absorbed and transferred inside the coupon by heat conduction.

In this model, the laser beam is considered as a rectangular-shaped laser spot (12 mm×1 mm) moving at a constant scanning speed, v (in millimeters per second) on the top surface of the coupon, and a uniform distribution (top-hat) of laser power, $\dot{q}$ (in watts per square millimeter), as described below [21]:

$$\dot{q} = \begin{cases} \frac{\eta P}{w\times l} & \text{for} \quad -\frac{w}{2} \le x \le \frac{w}{2}, \text{and} -\frac{l}{2} \le z - v.t \le l/2 \\ 0 & \text{for} \quad \text{others} \end{cases} \tag{4}$$

where, $P=\beta P_L$, β is the laser efficiency, η is the absorption coefficient, P_L is the laser power (W), w is the laser spot width (12 mm) along the x-axes of the coupon, and l is the laser spot length (1 mm) along the y-axes of the coupon.

The convection at the bottom surface of the coupon is described by Eq. 5:

$$k\frac{\partial T}{\partial z} = h_2(T - T_0) \tag{5}$$

where, h_2 is the natural convection coefficient at the bottom surface (in watts per square meter per degree Celsius).

The other surface boundary conditions are described by Eq. 6:

$$-k\frac{\partial T}{\partial n} = h_3(T - T_0) \tag{6}$$

where, $k\frac{\partial T}{\partial n}$ denotes the surface temperature gradient along normal direction n, h_3 is the natural convection coefficient (in watts per square meter per degree Celsius), and T is the surface temperature (°C).

3.4 Material properties and assumptions

In order to obtain a reasonable accuracy and computational efficiency, the following material properties and assumptions are incorporated in the model.

1. The base material (tool steel AISI S7) used in this work is assumed to be an isotropic, homogeneous, and temperature-dependent. The temperature-dependent thermal properties are summarized in Table 3.
2. A rectangular-shaped laser beam (12 mm×1 mm) with a uniform distribution (top-hat) of laser power $\dot{q}$ (in watts per square millimeter) moves along the scanning direction (y-axis) at a constant scanning speed, v (millimeters per second).
3. Direct diode laser efficiency (β=0.74) and absorptivity (η=0.69) are assumed to be constant [9, 21].

4. The coupon size is 50 mm×35 mm×10 mm, and the meshing element size is 0.025 mm for the heat-treated surfaces and a free meshing is used for other surfaces.
5. A quadratic, cube-shaped element (SOLID 70) with eight nodes is used to discrete the coupon's geometrical domain.
6. The heat transfer coefficients for forced convection (h_1) and natural convections (h_2 and h_3) are assumed to be 180 and 20 W/m^2 °C, respectively [22].

The FE analysis is carried out through a number of small time steps (Δt) with the time increment of 0.001 s. A number of iterations are performed to achieve a convergence criterion of 1% (the nodal temperature difference between two successive iterations). The flow chart of the FEM procedure is shown in Fig. 6.

4 Phase transformations and thermo-kinetic model

The iron-carbon phase diagram shown in Fig. 1b provides a valuable foundation to design the thermo-kinetic cycle taking place during the laser heat treatment process. The solubility of carbon in different phases with respect to temperature is shown in Fig. 1b. The high solubility of carbon in γ-iron can be utilized in the laser heat treatment process to achieve the desired surface properties. The laser heat treatment process takes place by austenization, homogenization, and quenching [2]. Several important critical temperatures (A_{C1}, A_{C3}, M_S, and M_F) are shown in Fig. 1b. The available empirical relationships from the literature [23–26] can be used to calculate the transformation temperatures (A_{C1}, P_S, and A_{C3}) and reaction temperatures (A_{r3}, A_{r1}, B_S, M_S, and M_F), as shown in Eqs. 7–14:

$$\begin{aligned} A_{C1} = {} & 723 - 7.08\,Mn - 37.7\,Si - 18.1\,Cr + 44.2\,Mo \\ & + 8.95\,Ni + 50.1\,V + 21.7\,Al + 3.18\,W + 297\,S - 830\,N \\ & - 11.5\,C \times Si - 14.0\,Mn \times Si - 3.10\,Si \times Cr - 57.9\,C \\ & \times Mo - 15.5\,Mn \times Mo - 5.28\,C \times Ni - 6.0\,Mn \times Ni \\ & + 6.77\,Si \times Ni - 0.80\,Cr \times Ni - 27.4\,C \times V + 30.8\,Mo \\ & \times V - 0.84\,Cr^2 - 3.46\,Mo^2 - 0.46\,Ni^2 - 28\,V^2 \end{aligned} \quad (7)$$

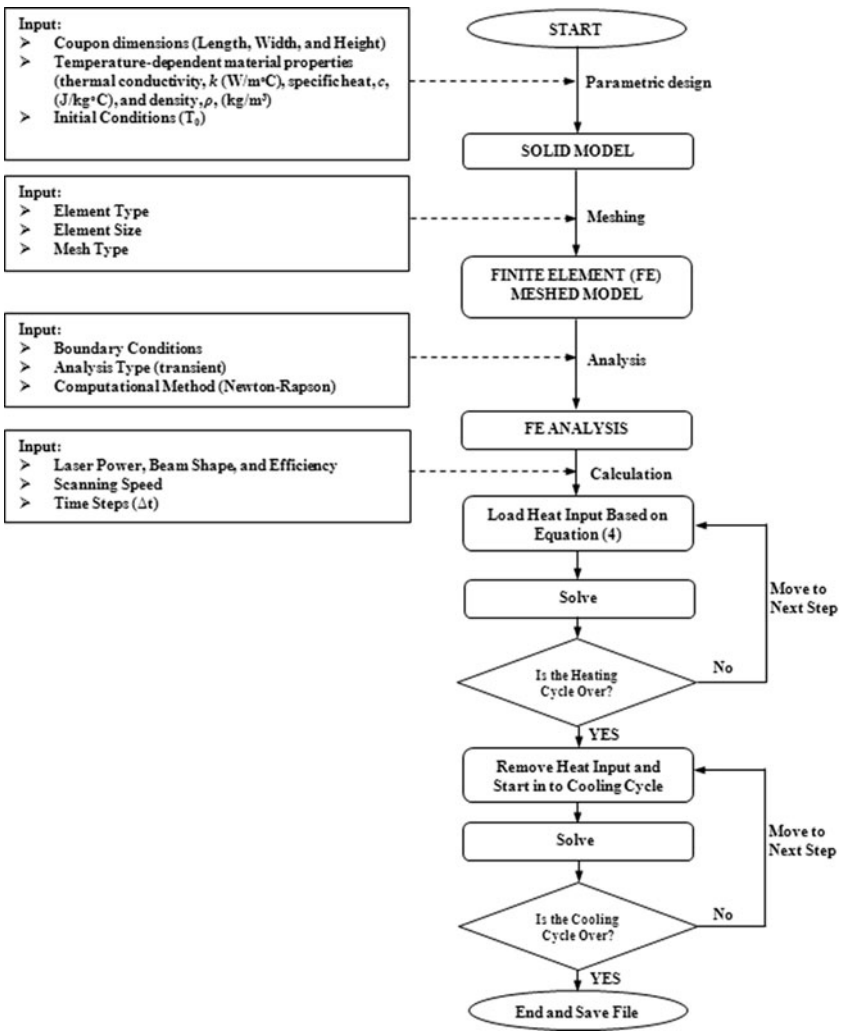

Fig. 6 Flow chart of the FEM procedure for thermal analysis

$$A_{C3} = 910 - 370\,C - 27.4\,Mn + 27.3\,Si - 6.35\,Cr - 32.7\,Ni + 95.2\,V + 190\,Ti + 72.0\,Al + 64.5\,nb + 5.57\,W + 332\,S + 276\,P + 485\,N - 900\,B + 16.2\,C \times Mn + 32.3\,C \times Si + 15.4\,C \times Cr + 48.0\,C \times Ni + 4.32\,Si \times Cr - 17.3\,Si \times Mo - 18.6\,Si \times Ni + 4.80\,Mn \times Ni + 40.5\,Mo \times V + 174\,C^2 + 2.46\,Mn^2 + 6.86\,Si^2 + 0.322\,Cr^2 + 9.90\,Mo^2 + 1.24\,Ni^2 - 60.2\,V^2 \quad (8)$$

$$P_S = A_{C1} - 10.7\,Mn + 29\,Si + 16.9\,Cr \quad (9)$$

$$A_{r3} = 910 - 310\mathrm{C} - 80\mathrm{Mn} - 20\mathrm{Cu} - 15\mathrm{Cr} - 55\mathrm{Ni} - 80\mathrm{Mo} + 0.35(h - 8) \quad (10)$$

$$A_{rl} = P_S - 305.4\mathrm{C} - 118.2\mathrm{Mn} \quad (11)$$

$$B_S = P_S - 58\mathrm{C} - 35\mathrm{Mn} - 15\mathrm{Ni} - 34\mathrm{Cr} - 41\mathrm{Mo} \quad (12)$$

$$M_s = 561 - 474\mathrm{C} - 33\mathrm{Mn} - 17.7\mathrm{Ni} - 12.1\mathrm{Cr} - 7.5\mathrm{Mo} + 10\mathrm{Co} - 11\mathrm{Si} + 230 \quad (13)$$

$$M_F = M_S - 215 \quad (14)$$

where, C, Mn, Cr, Mo, etc., are steel composition in wt%, and h is the thickness (mm) of the material.

The phase transformation model used in this work is based on the original model developed by Kirkaldy et al. [27] and on the modified model proposed by Li et al. [28]. The volume fraction of the transformed phases (ferrite, pearlite and bainite) can be calculated by Eq. 15:

$$X = \int_0^t \frac{\Delta T^n \exp\left(-\frac{Q}{RT}\right) X^{0.4(1-X)}(1-X)^{0.4X}}{F(\mathrm{C,Mn,Si,Ni,Cr,Mo},G)} \quad (15)$$

where, the denominator refers to the steel composition in wt%, ΔT (°C) is the undercooling, n is the constant (n=2 for volume and n=3 for boundary), Q (J) is the activation energy, R, is the gas constant, T (°C) is the instantaneous temperature, G is the ASTM grain size number and t is time (in seconds).

The carbon diffusion and martensite decomposition are mostly dependent on the activation energy (Q) involved in the process [10]. The activation energy can be calculated by solving the following differential equation (Eq. 16) as described below [28]:

$$\frac{d}{dT}\left(\Delta T^n \exp^{\left(-\frac{Q}{RT}\right)}\right) = 0 \quad (16)$$

which leads to the following relationship:

$$Q_{\max} = \frac{nRT^2}{\Delta T} \quad (17)$$

Equations 18–20, proposed by Li et al. [28] are used to calculate the ferrite, pearlite, and bainite phase compositions as described below:

$$\text{Ferrite composition} = \exp(1.00 + 6.31\mathrm{C} + 1.78\mathrm{Mn} + 0.31\mathrm{Si} + 1.12\mathrm{Ni} + 2.70\mathrm{Cr} + 4.06\mathrm{Mo}) \quad (18)$$

$$\text{Pearlite composition} = \exp\left(-4.25 + 4.12\mathrm{C} + 4.36\mathrm{Mn} + 0.44\mathrm{Si} + 1.71\mathrm{Ni} + 3.33\mathrm{Cr} + 5.19\sqrt{\mathrm{Mo}}\right) \quad (19)$$

$$\text{Bainite Composition} = \exp(-10.23 + 10.18\mathrm{C} + 0.85\mathrm{Mn} + 0.55\mathrm{Ni} + 0.90\mathrm{Cr} + 0.36\mathrm{Mo}) \quad (20)$$

An empirically based equation (Eq. 21) proposed by Koinstinen and Marburger [29] can be used to calculate the proportion of martensite as follows:

$$X_M = 1 - X_A \exp[-0.011(M_S - T] \quad M_S > T > M_F \quad (21)$$

where, X_M and X_A are the volume fraction (in percent) of the martensite and austenite phases, M_S and M_F are the martensite starting and ending temperatures (in degrees Celsius), and T is the instantaneous temperature (in degrees Celsius).

Equations 22–24 proposed by Maynier et al. [30] are used to calculate the hardness of martensite (HV_M), bainite (HV_B), and mixture of ferrite and pearlite (HV_{F+P}), as shown below:

$$HV_M = 949C + 27Si + 11Mn + 8Ni + 16Cr + 21(\log T_t) \quad (22)$$

$$HV_B = -123 + 185C + 330Si + 153Mn + 65Ni + 144Cr + 191Mo + (89 + 53C - 55Si - 22Mn - 10Ni - 20Cr - 33Mo)\log T_t \quad (23)$$

$$HV_{F+P} = -223C - 53Si - 30Mn - 12.6Ni - 7Cr - 19Mo + (10 - 19Si + 4Ni - 8Cr + 130V)\log T_t \quad (24)$$

where, $\log T_t$ is the critical cooling time determined from the T_{AUS} to M_S temperatures that can be calculated as the function of carbon equivalent [28], as shown in Eqs. 25 and 26:

$$\log(T_t) = 10.6\, C_E - 4.8 \quad (25)$$

$$C_E = C + \frac{Mn}{6} + \frac{Mo}{4} + \frac{Cr}{8} + \frac{Ni}{12} + \frac{Si}{24} + \frac{Cu}{15} \quad (26)$$

The total hardness [30] can be calculated based on a rule of mixture, as shown in Eq. (27):

$$HV = X_M HV_M + X_B HV_B + X_{F+P} HV_{F+P} \quad (27)$$

5 Results and discussion

5.1 Temperature distribution and geometry characterization of multi-pass heat-treated coupons

In many published works [9, 11–18], HPDDL is demonstrated as an ideal heat source for localized heat treatment. The laser beam profile (circular, square, or rectangular) and the corresponding distribution of laser power (Gaussian or top-hat) are important characteristics to achieve the desired temperature distribution, phase transformations, and hardness [18]. Therefore, the final depth of heat treatment and hardness are dependent on the applied heat input and the relevant quenching capability (cooling rate) [22]. In this study, the process parameters shown in Table 4 are used. Initially, as a rule of thumb, the length of scan was set two times (25 mm) of the laser spot width (12 mm) [6, 11]. The FE meshed model is shown in Fig. 7.

The numerical simulation procedures presented in Section 3.2 are used to obtain the variation of temperature of the heat-treated coupons with respect to change in time. The micrograph at magnification of ×50 shown in Fig. 14a is used to measure the depth of heat treatment (D). A digital microhardness tester with the loading of 200 gf and dwelling time of 15 s are used to measure the hardness. The hardness measurement pattern is shown in Fig. 14a. In Fig. 14a, the hardness measurement is performed below 25 μm from the top surface of the heat-treated coupon across the first track, the overlapped region, and the second track. In addition, the hardness along the center of the first track, the center of the overlapped region, and the center of the second track is also measured. The measured hardness distribution across the surface and the cross-section of the multi-pass heat-treated coupon at the laser power of 1,600 W, scanning speed of 20 mm/s, size of overlap of 3 mm, and length of scan of 20 mm is shown in Fig. 13d–e. The detailed numerical simulation results of temperature and the measured depth of heat treatment and hardness of the heat-treated coupons for various processing parameters are summarized in Table 4. In Table 4, the reported values of hardness are the average ones across the first track, the overlapped region, and the second track of the heat-treated coupons.

As mentioned in the introduction, the industry imposed the laser heat treatment process specifications in terms of depth of heat treatment and magnitude of hardness. Therefore, in the case of MPLHT, a minimum variation of hardness across the depth of heat treatment should be achieved. In this study, a smaller group of Exps. 8, 11, 14, 16, 17, 18, and 26 shown in Table 4 representing the different heat treatment processing parameters such as laser power, scanning speed and size of overlap that are taken for analysis. Exp. 26 shown in Table 4 produces an uneven depth of heat treatment (180→160 μm) and a non-uniform hardness distribution between the tracks and the overlapped region (765→726 HV). The non-uniform hardness distribution across the depth of heat treatment could be the result of excessive heat generated and a minimum/uneven cooling rate due to the higher laser power (1,800 W) with lower scanning speed (15 mm/s) [18]. The results for Exps. 8, 11, 14, and 18 that are recorded in Table 4 show larger variations in the depth of heat treatment (140→120 μm, 135→95 μm, 145→125 μm, and 150→130 μm) and larger variations in hardness (648→608 HV, 662→621 HV, 684→651 HV, and 663→609 HV). The larger variation in hardness across the depth of heat treatment could be the result of the lower laser power (1,400 W), higher scanning speed (25 mm/s), or minimum size of overlap (1 and 2 mm). In Table 4, a minimum variation in hardness across the depth of heat treatment is achieved under the following processing windows corresponding to the Exps. 7, 17, and 27: laser power (1,400–1,800 W), scanning speeds (15–25 mm/s), and size of overlap of 3 mm.

In the MPLHT process, the uniformity of hardness distribution across the depth of heat treatment is dependent on the tempering temperature generated during the successive scans of laser beam over the previously heat-treated area [16]. The heat input and the transformation/interaction time

Table 4 Numerical simulation results of temperature (°C) and measured depth of heat treatment (μm) and hardness (HV) for various process parameters

Ex #	Laser power (W)	Scanning speed (mm/s)	Overlap (mm)	T (°C)		D (μm)		Hardness (kgf/mm^2)	
				T_{TR}	T_{OV}	D_{Tr}	D_{OV}	HV_{Tr}	HV_{OV}
1	1,400	15	1.0	917	882	125	90	616	590
2	1,400	20	1.0	869	837	110	75	580	561
3	1,400	25	1.0	824	785	105	60	543	497
4	1,400	15	2.0	928	908	135	120	632	603
5	1,400	20	2.0	912	864	125	110	607	576
6	1,400	25	2.0	831	808	115	105	551	509
7	1,400	15	3.0	984	953	155	145	661	638
8	1,400	20	3.0	948	914	140	120	649	608
9	1,400	25	3.0	910	813	130	110	605	536
10	1,600	15	1.0	1,002	952	140	105	683	650
11	1,600	20	1.0	986	924	130	95	662	621
12	1,600	25	1.0	927	901	125	80	631	592
13	1,600	15	2.0	1,013	998	160	135	696	679
14	1,600	20	2.0	1,007	956	145	125	684	651
15	1,600	25	2.0	941	913	135	110	640	606
16	1,600	15	3.0	1,093	1,042	185	160	765	721
17	1,600	20	3.0	1,029	1,018	160	155	728	714
18	1,600	25	3.0	992	917	150	130	663	609
19	1,800	15	1.0	1,020	963	155	115	709	656
20	1,800	20	1.0	1,015	937	140	105	698	639
21	1,800	25	1.0	998	925	130	100	679	621
22	1,800	15	2.0	1,033	1,009	170	145	717	688
23	1,800	20	2.0	1,016	994	155	135	703	663
24	1,800	25	2.0	1,010	929	145	130	689	635
25	1,800	15	3.0	1,136	1,059	195	170	791	732
26	1,800	20	3.0	1,090	1,049	180	160	765	726
27	1,800	25	3.0	1,024	999	160	150	712	699

T_{TR} average temperature at track, T_{OV} average temperature at overlap, D_{TR} average depth of heat treatment at track, D_{OV} average depth of heat treatment at overlap, HV_{TR} average hardness at track, HV_{OV} average hardness at overlap

play a major role to determine the variation of surface temperature, tempering temperature, phase transformations, microstructure formation, and hardness of the MPLHT process [11, 15, 16]. The heat input shown in Eq. 4 is the function $[f(\dot{q}) = f(P, l, w, \beta, \eta)]$ of laser power (P, in watts), length of laser spot (l, in millimeters), width of laser spot (w, in millimeters), laser efficiency (β, in percent), and absorption coefficient (η, in percent) of the laser beam to the material. The transformation time, $\left[t_i(\mathrm{s}) = \frac{L_s(\mathrm{mm})}{v\left(\frac{\mathrm{mm}}{\mathrm{s}}\right)}\right]$ is defined as the ratio between the length of scan (L_S, in millimeters) and the scanning speed (v, in millimeters per second) [11, 16]. If the heat input and the scanning speed are constant for a specific size of overlap (i.e., O_V=25% of the width (w, in millimeters) of laser beam [10, 11, 15–18]), then, the length of scan can be used to obtain the variation of tempering temperature. The variation of tempering temperature is used to obtain the change of phase transformations, the microstructure formation, and the hardness distribution across the depth of heat treatment [15].

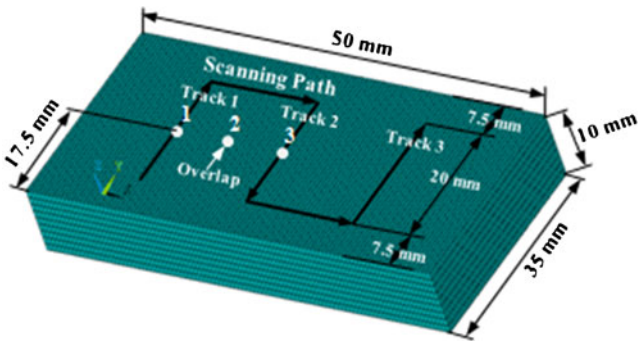

Fig. 7 Meshed finite element model of the coupon

In this study, the processing parameters of Exp. 17 shown in Table 4 and the lengths of the scan shown in Table 5 are used. The effect of the lengths of scan on the variation of temperature including the tempering temperature, the time taken for heating and cooling cycles, and the values of hardness are summarized in Table 5. In Fig. 8a–c, the schematic presentation of different lengths of scan such as,

Table 5 The effect of length of scan on the evolution of surface temperature, transformation time and hardness of the MPLTH process

Ex #	L_S (mm)	T (°C)			t (s)			$HV_{0.2}$ (kgf/mm^2)		
		T_{Tr}	T_{Ov}	T_{temp}	t_i	t_h	t_c	HV_{Tr}	HV_{Ov}	ΔHV
1	10	1,015.31	1,034.77	884	0.5	0.125	0.375	739	562	177
2	15	1,012.39	1,024.31	809	0.75	0.125	0.625	733	619	114
3	20	1,019.81	1,015.64	737	1.0	0.15	0.85	728	712	16
4	25	1,021.35	1,009.40	662	1.25	0.15	1.1	717	605	112
5	30	1,021.56	1,005.79	608	1.5	0.15	1.35	708	544	164
6	35	1,022.38	1,002.47	585	1.75	0.175	1.575	694	483	211

L_S length of scan, T_{TR} average temperature at track, T_{OV} average temperature at overlap, T_{temp} tempering temperature at overlap, t_i transformation/interaction time, t_h time taken for heating, t_c time taken for cooling, HV_{TR} average hardness at track, HV_{OV} Average hardness at overlap, ΔHV= HV_{TR}~HV_{OV}

10 mm, 20 mm, and 30 mm are shown. The numerical simulation of temperature distribution at the points 1 to 3 marked in Fig. 8a–c are shown in Fig. 8d–f. The measured hardness distribution below 25 μm from the top surface of the heat-treated coupons across the depth of heat treatment is shown in Fig. 8g–i. In Table 5, it can be seen that the overlapped region temperature and the tempering temperature are decreasing linearly with the increase in length of scan. In contrast, the time of cooling cycle (t_c) increases with the increase in the length of scan.

In Table 5, the length of scan is below 20 mm, the tempering temperature is achieved above A_{C1} temperature, the length of scan is above 20 mm, and the transformation temperature is achieved below A_{C1} temperature. At the lengths of scan of 10 and 15 mm, the time $[t < t_{\alpha^1}]$ taken for diffusion of carbon in the austenite is not enough (see Fig. 1c) to fully transform into martensite [10, 15]. Therefore, a portion of retained austenite is mixed with martensite that reduced (ΔHV>100 kgf/mm^2) the hardness at the overlapped region. For the lengths of scan of 25, 30, and 35 mm, the tempering temperature is achieved below the A_{C1} temperature and the time $[t < t_{\alpha^1}]$ allowed for diffusion of carbon in the austenite is passed through the noses of the bainite, ferrite, and pearlite phases shown in Fig. 1c [5]. In those lengths of scan, a larger variation of hardness (ΔHV> 160 kgf/mm^2) across the depth of heat treatment is achieved due to a mixture of the phases of bainite, ferrite, and pearlite with martensite. A minimum hardness variation (ΔHV< 20 kgf/mm^2) across the depth of heat treatment is achieved at the length of scan of 20 mm. In this length of scan, a balanced thermal cycle $[f(T, t)=f(L_S)]$ is achieved for a fully martensite transformation during the MPLHT process. It can be concluded that in the MPLHT process, the variation of hardness is a function $[f(HV)=f(T_{temp})]$ of the tempering temperature (T_{temp}, in degrees Celsius). Whereas, the tempering temperature is a function $[f(T_{temp})=f(L_S)]$ of the length of scan (L_S, in millimeters). Therefore, in the MPLHT process, the hardness uniformity is a function $[f(HV)=f(L_S)]$ of length of scan (L_S, in millimeters).

The surface temperature distribution of the heat-treated coupon obtained from the FE thermal model at the laser power of 1,600 W, the scanning speed of 20 mm/s, the size of overlap of 3 mm, and the length of scan of 20 mm for various time frames is shown in Fig. 9. In Fig. 9, the maximum temperatures of the first, second, and third tracks at the starting (0.05, 1.5, and 3.0 s), middle (0.5, 2.0, and 3.5 s) and ending (1.0, 2.5, and 4.0 s) time frames are: 989, 1,038, and 1,047°C; 990, 1,016, and 1,023°C; 991, 1,007, and 1,015°C, respectively. In Fig. 9, it can be seen that the accumulated heat from the previous track could increase the later track temperature at the starting position [9, 22]. The initial temperature rise of the second track of about 47°C (1,038–991°C) is due to the effect of heat accumulation from the first track. This heat accumulation effect decreases at the middle of the track for about 25°C (1,016–991°C) and at the end of the track for about 16°C (1,007–991°C) of the second track. A similar trend is observed during the third track. In Fig. 9, the predicted maximum temperature is above the austenization temperature (940°C) of tool steel AISI S7, but below the melting temperature (1,438°C) [5]. Therefore, a full austenization is achieved without melting the surface [9].

The cross-sectional temperature distribution of the heat-treated coupon obtained from the FE thermal model at the laser power of 1,600 W, scanning speed of 20 mm/s, size of overlap of 3 mm, and length of scan of 20 mm with different time frames is shown in Fig. 10. The average temperature distribution of three tracks (Fig. 10) along the depth of the heat-treated coupon is shown in Fig. 11. The calculated values of transformation temperatures (A_{C3}, P_S, A_{C1}, B_S, and M_S) of tool steel AISI S7 are shown in Fig. 11. The values of cross-sectional temperatures at the distances from 0 μm to 600 μm with an increment of 50 μm are: 1,019, 998, 974, 942, 896, 821, 729, 593, 455, 381, 335, 294, and 246°C, respectively. In Fig. 11, due to the variation in transformation temperatures ($A_{C1}\rightarrow A_{C3}$), three modes of austenization are achieved along the depth of the heat-treated coupon. A full austenization is achieved up to 155 μm of the depth of heat treatment in the heat-treated

zone (HTZ). A partial austenization is achieved below the HTZ and in the HAZ. The bulk mass of the material acts as a heat sink; therefore, a drastic variation of temperature is achieved below 155 μm of the depth of the heat-treated coupon. A 145 μm depth of HAZ and a 300 μm depth of the transition zone (TZ) are achieved. Below the TZ, the temperature is observed to be less than M_F temperature and the microstructure of the base material (BM) is not affected by the heat.

The FE thermal model results are compared with the thermocouple temperature measurements. The thermocouples set locations are shown in Fig. 4c. The cross-sectional temperatures measured by thermocouples at 0.5 mm below the top surface of the heat-treated coupon and the same location FE thermal model results are shown in Fig. 12. The maximum temperatures measured by thermocouples at the center of the first track, the center of the overlapped zone and the center of the second track are 311, 313, and 312°C, respectively. The same location FE thermal model results are 322, 326, and 323°C, respectively. The mean error between the FE thermal model and the experimental results is about 3.59%. The

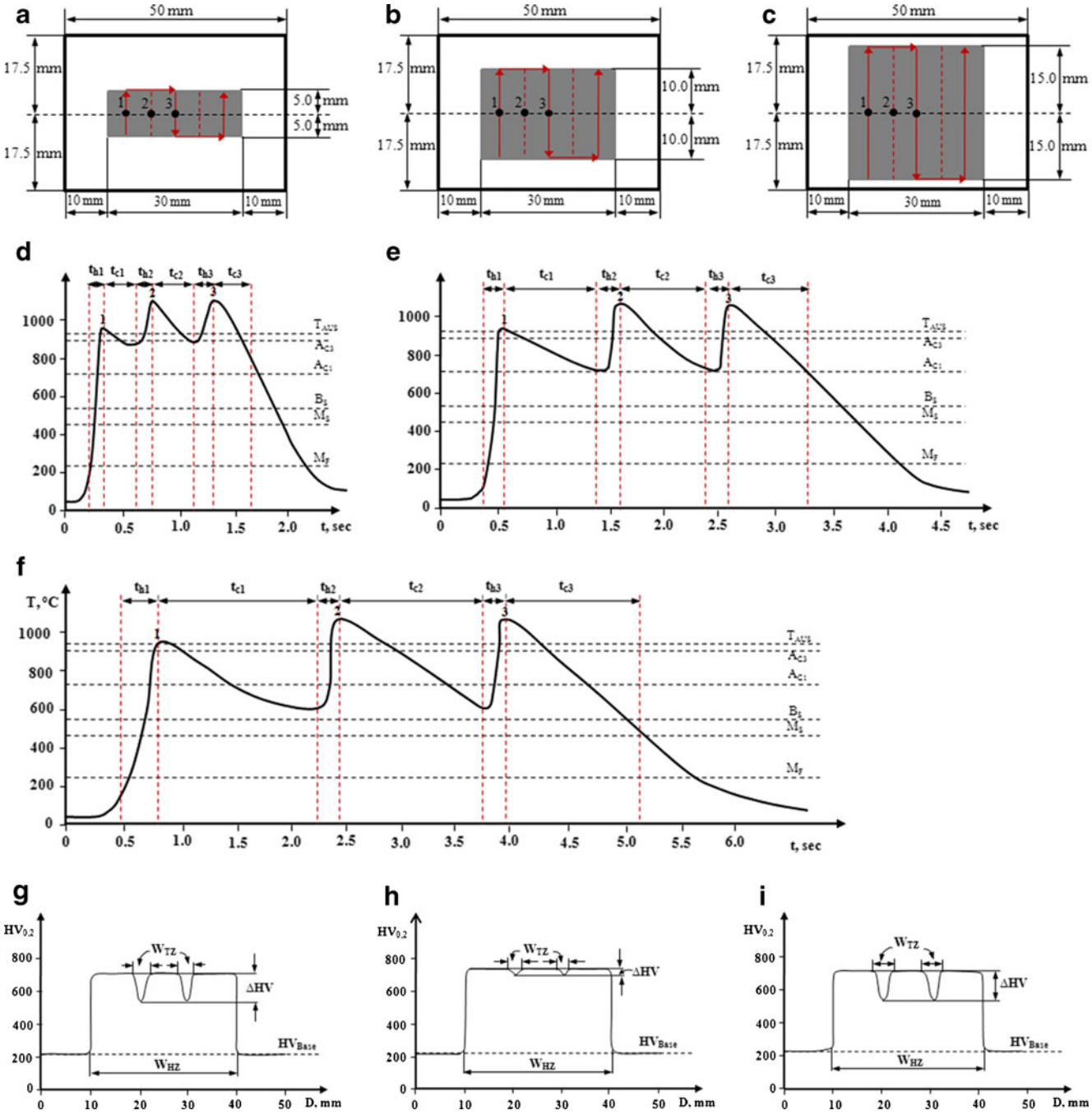

Fig. 8 The effect of length of scan (**a**–**c**) on the evolution of temperature (**d**–**f**) and hardness (**g**–**i**)

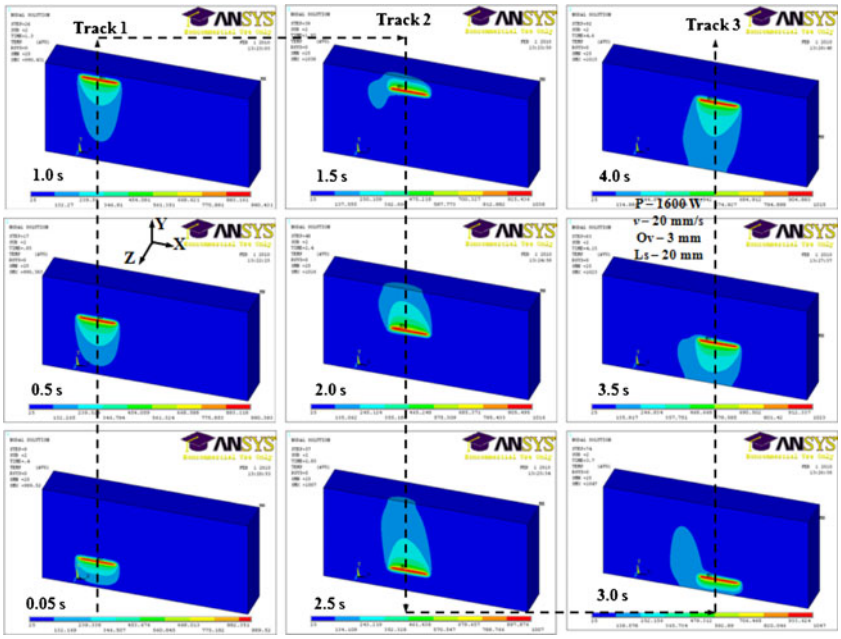

Fig. 9 The top surface temperature distributions obtained from the FE thermal model for various time frames of Experiment 17 shown in Table 4

minimum error shows that the FE thermal model results are reliable and computationally efficient. Therefore, the FE thermal model can be used to predict the cross-sectional as well as surface temperature history of multi-pass laser heat treatment for any given process parameters.

5.2 Phase transformation, hardness distribution, and microstructure characterization

In the laser heat treatment process, the localized hardening is achieved through phase transformation. Therefore, the final hardness is dependent on the phase changes caused by the level of carbon solubility during the heating and cooling cycles. The temperature history acquired from the FE thermal model shown in Fig. 10 is coupled with Eq. 17 to calculate the activation energies (Q) for the austenite, bainte, ferrite, and pearlite phases. The calculated average values of activation energies for austenite, banite, ferrite and pearlite are 157, 134, 112, and 86 kJ/mol, respectively. The calculated values are in good agreement with literature values [9, 14]. The undercooling (ΔT) for austenite, ferrite, pearlite and bainite are: 139, 101, 120, and 150 (°C), respectively [27]. The calculated values of hardness of martensite, bainite, and a mixture of ferrite and pearlite obtained from Eqs. 22–24 are: 793, 560, and 354 HV, respectively. The numerical values of temperature obtained from the FE thermal model

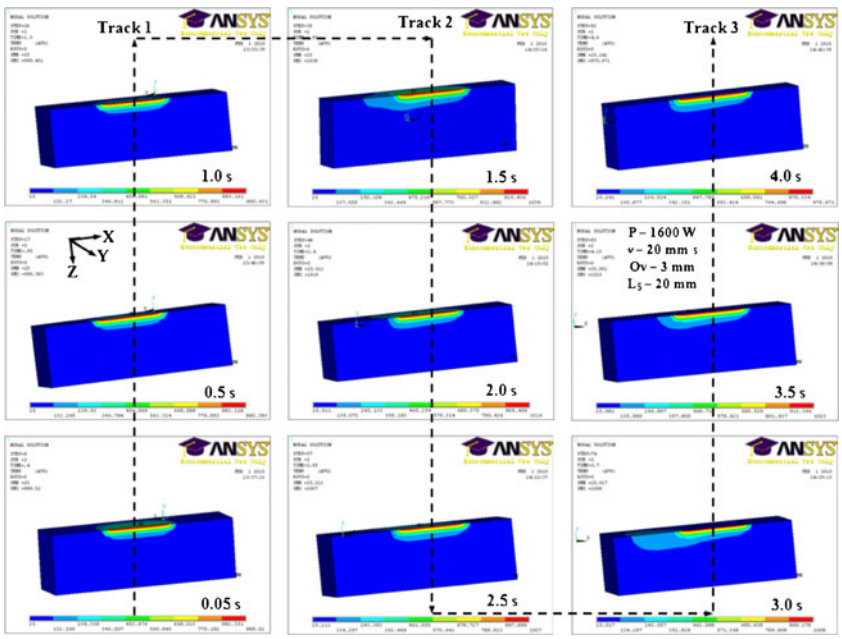

Fig. 10 The cross-sectional temperature distribution obtained from the FE thermal model for various time frames of Experiment 17 shown in Table 4

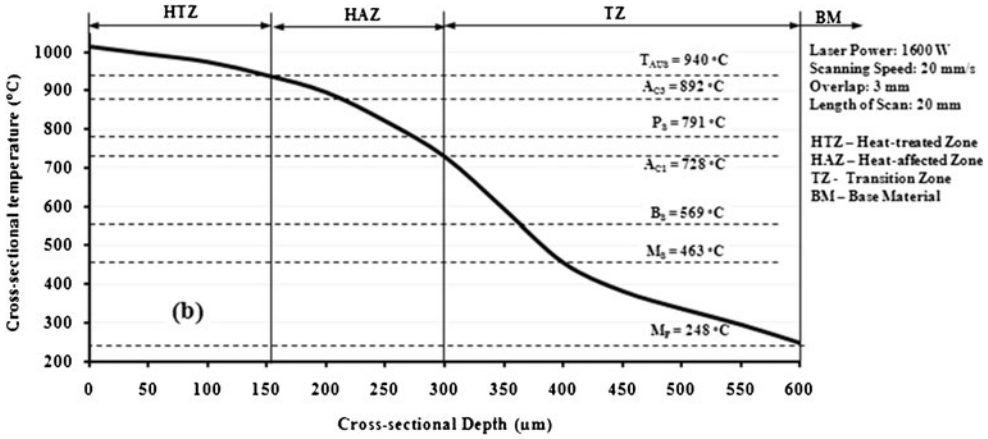

Fig. 11 The average cross-sectional temperature vs cross-sectional depth of the coupon of Experiment 17 shown in Table 4

shown in Figs. 9, 10, and 11, the calculated values of activation energies (Q), and the undercooling values (ΔT) for bainte, ferrite, and pearlite are plugged in Eq. 15 to calculate the volume fractions of phases generated by the decomposition of austenite. The corresponding final hardness values are shown in Table 6.

In Fig. 13a, the thermal cycles denoted by 1, 2, and 3 are the thermal history obtained from the FE thermal model at locations 1, 2, and 3 shown in Fig. 7 during the multiple scans of laser beam over the first track, the overlapped region, and the second track. The overlapped region (location 2 shown in Fig. 7) thermal cycles during the first, second, and third tracks are marked as 2^{1}, 2^{11}, and 2^{111}, as shown in Fig. 13b. In Fig. 13b, the new heating cycle during the second track (2^{11}) starts before ending the first track of the cooling cycle at 754°C denoted by 2^{1}_{C}, clearly indicating that the overlapped region temperature is maintained above the A_{C1} temperature. At the end of the second track, the cooling cycle is almost reached (denoted by 2^{11}_{C} shown in Fig. 13b) near room temperature (RT). A small increase in temperature about 150°C (denoted by 2^{111} shown in Fig. 13b) is achieved during the new heating cycle (t_{3h}) of the third track. Refer to Figs. 1b–c and 8e for temperature (150°C) and the time (1.5 s) taken for the cooling cycle that could generate a ε-carbide microstructure in the overlapped region [5–7, 12]. The formation of ε-carbide with the mixture of martensite in the overlapped region results in a hardness reduction (see Fig. 13d) across the depth of heat treatment in the MPLHT process. However, the accumulated heat from the previous pass could be effectively used in this model during the multiple scans of laser beam in order to minimize the tempering effect, which ultimately produces a minimum variation of hardness across the heat-treated depth of material.

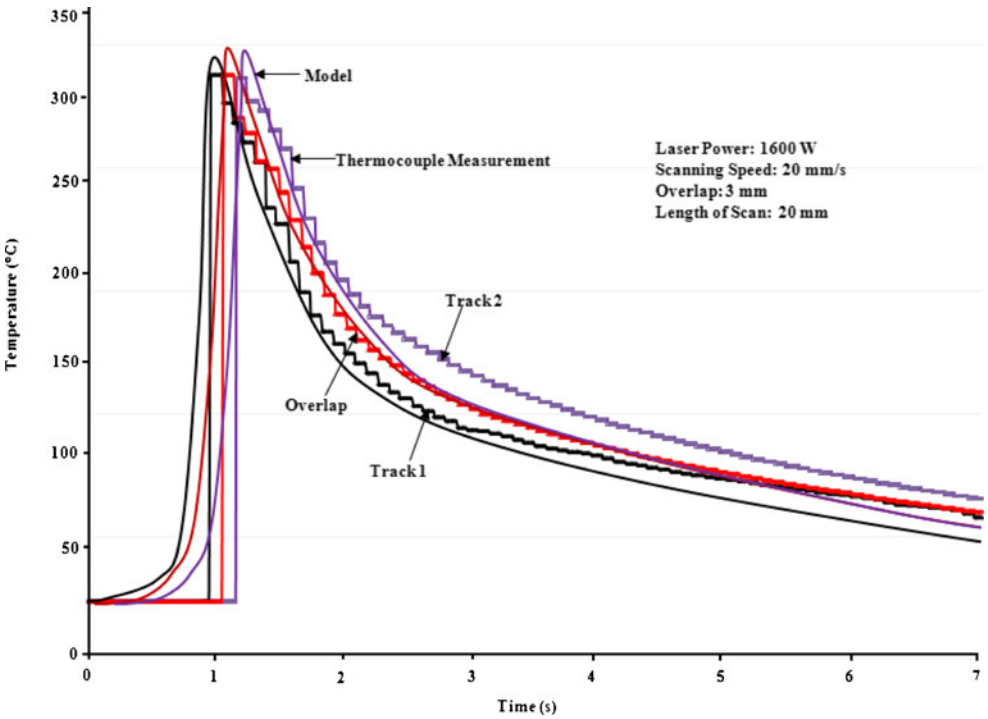

Fig. 12 Comparison of temperatures measured by thermocouple with respect to temperature obtained by numerical simulation

Table 6 The calculated final hardness with respect to volume fractions of martensite, bainite, pearlite and ferrite at different time scales

Time (*s*)	Volume fractions (%)			Hardness (kgf/mm^2)
	Ferrite+Pearlite	Bainite	Martensite	
0.65	0.09	0.14	0.27	324
1.0	0.06	0.08	0.52	478
1.45	0.03	0.04	0.74	620
1.9	0.01	0.01	0.93	747
2.5	0.01	0.01	0.94	755
3.75	0.01	0.01	0.945	759

The thermal cycles obtained from the FE thermal model, shown in Fig. 13a, are coupled with Eq. 21 to simulate the austenite→martensite phase transformation. The simulated martensite phase transformation is shown in Fig. 13c. In this phase transformation model, a cumulative time approach is used for the phase transformations. In Fig. 13c, during the scan of laser beam at the first track, the austenization starts at 0.65 s and ends at 1.25 s; the homogenization takes place between 1.25 and 1.3 s; followed by quenching, starting at 1.3 s and ending at 2.4 s. During the overlapping of 3 mm with the 12-mm-width of laser beam, the austenization starts at 1.25 s and ends at 1.85 s; and the homogenization is completed between 1.85 and 1.9 s. The quenching takes place between 1.9 and 3.0 s. During the scan of the laser beam at the second track, the austenization starts at 2.4 s and ends at 3.0 s. Further homogenization is completed between 3.0 and 3.05 s, followed by quenching from 3.05 to 4.15 s.

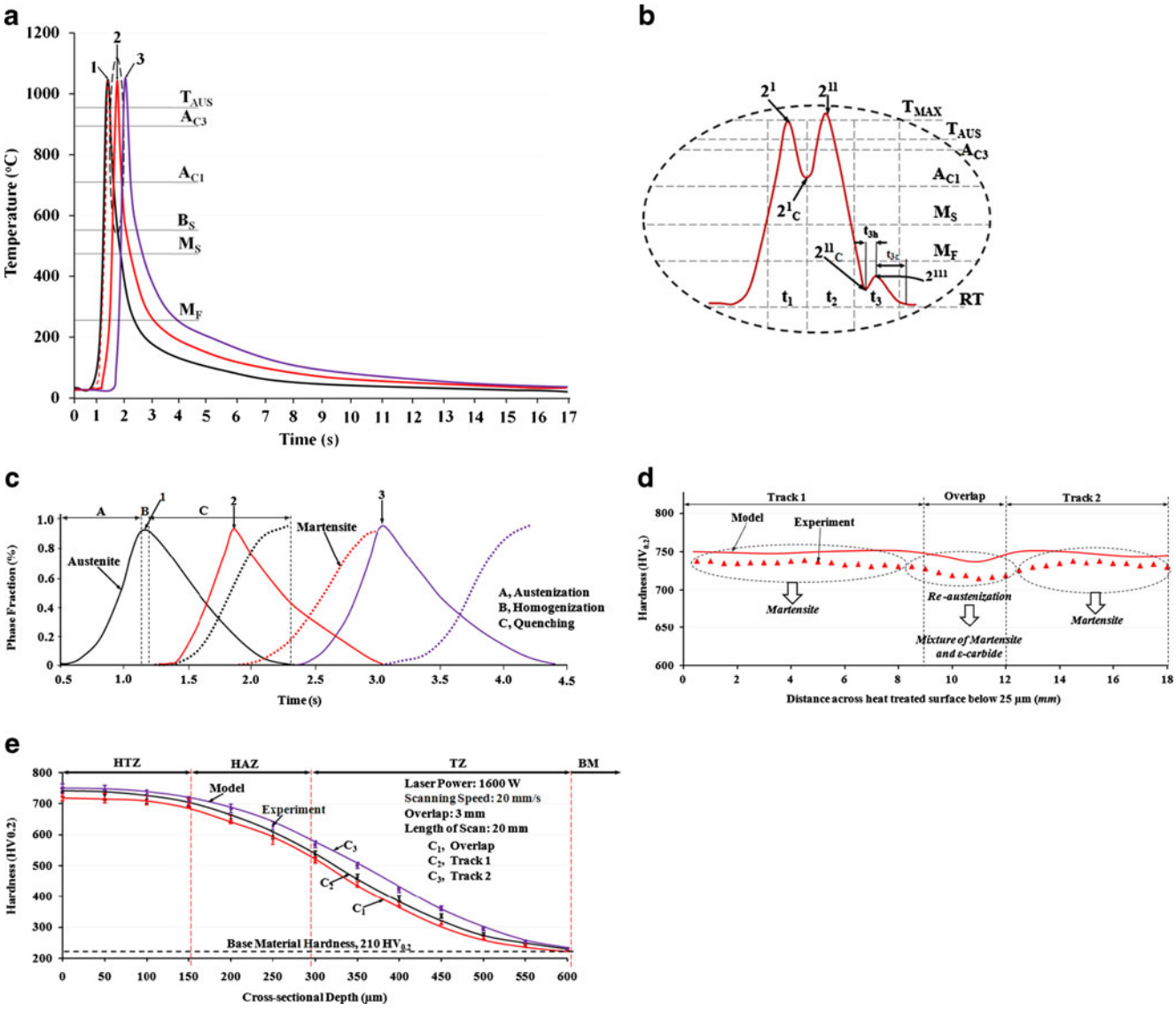

Fig. 13 Phase transformation model using Experiment 17 processing parameters **a** thermal cycle **b** overlapped region thermal cycle **c** austenite→martensite phase transformation cycles, predicted and measured hardness distributions **d** across the depth of heat treatment, and **e** along the cross-section of the coupon

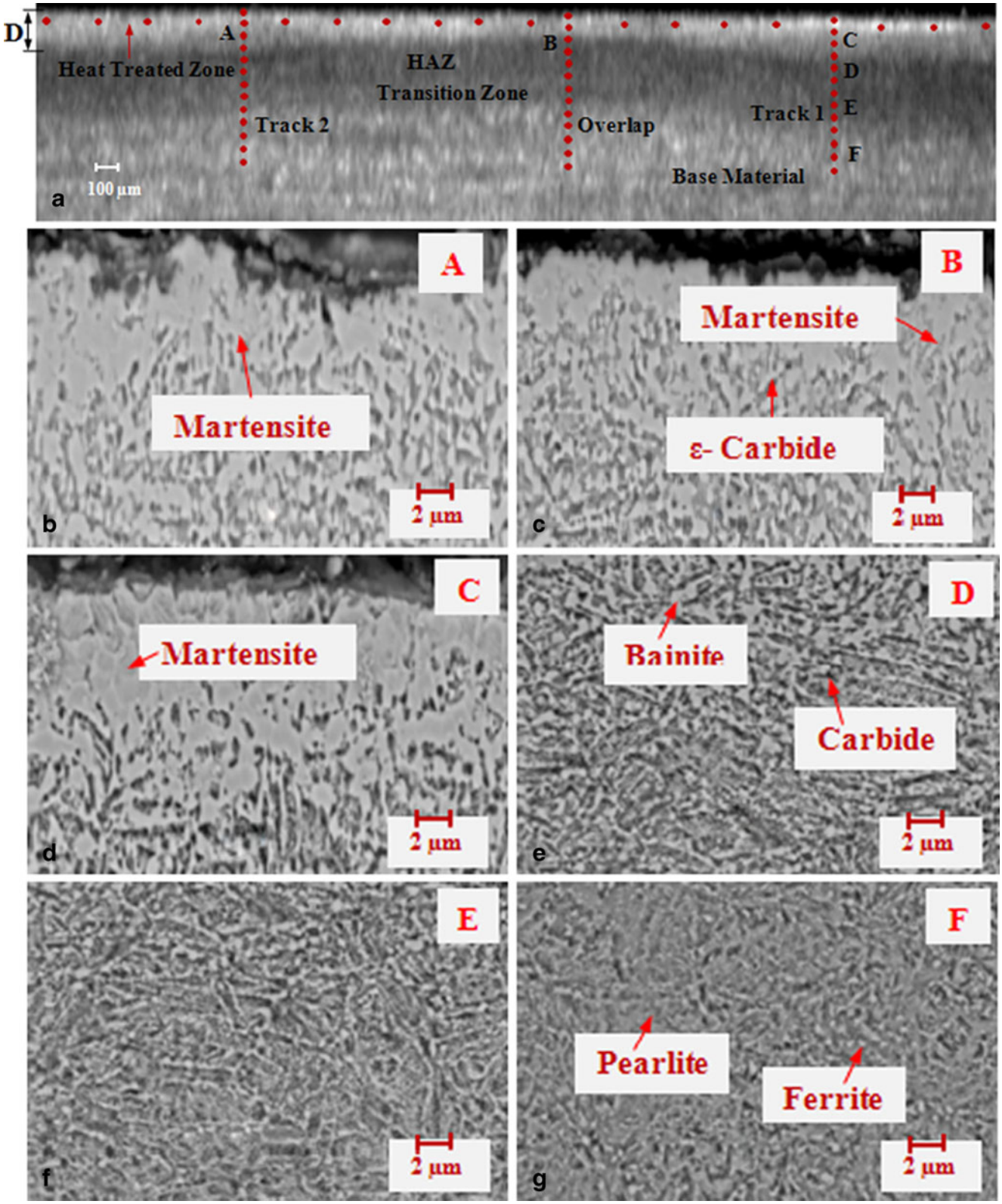

Fig. 14 Micrographs of multi-track laser heat treatment **a** at magnification of ×50 **b**–**g** at magnification of ×2,000, heat-treated zone of **b** first track, **c** overlapped region and **d** second track **e** HAZ **f** transition zone, and **g** base material

The predicted and measured hardness distribution below 25 μm from the top surface of the first track, the overlapped region and the second track is shown in Fig. 13d. In Fig. 13d, a similar trend in hardness distribution across the

depth of heat treatment between the predicted and measured data could be observed. A small decrease in hardness observed in the overlapped region with respect to the first and second tracks. The thermal cycles evolved in the overlapped region (see Figs. 13b and 14d–f) during the multiple scans of laser beam generate a mixture of tempered microsturcture with martensite [6–10, 31]. The portion of tempered microstructure with martensite varies with respect to the tempering temperature and time [6, 7, 12]. In this case, the predicted tempering temperature (denoted by 2^{111} shown in Fig. 13b) is about 150°C, and the time taken for cooling is about 1.5 s. In this temperature and time (see Figs. 1b–c), ε-carbide could be formed as a decomposed product from the martensite during the reasutenization of the MPLHT process [5–8]. The thermo-kinetic analysis is verified with the micrograph shown in Fig. 14c. The mixture of tempered microstructure (ε-carbide) with martensite shows a reduction in hardness in the overlapped region with respect to the first and second tracks.

The cross-sectional micrographs (×50) of the heat-treated coupon along the locations 1, 2, and 3 marked in Figs. 4c and 7 are shown in Fig. 14a. The higher magnification (×2,000) micrographs of the locations from A to F, shown in Fig. 14b–g, can be used to characterize the formation of the microstructure as a function of thermal cycles (see Fig. 13a–b). The predicted and measured hardness values along the cross-section of the first track, the second track, and the overlapped region are plotted in Fig. 13e. In Figs. 13e and 14, four different zones such as the HTZ, HAZ, TZ, and BM could be distinguished.

In Fig. 13e, the curves denoted by C_1, C_2 and C_3 are the hardness distributions in the cross-section of the overlapped region, the first track, and the second track, respectively. In Fig. 13e, the average hardness value of the first track and the second track in the HTZ is 729 and 737 HV, respectively. The difference of the hardness values in the HTZ of the first and second tracks could be caused by the variation of the percentage of martensite present in that zone (see Fig. 14b and d). A mixture of martensite and ε-carbide that is present in the HTZ of the overlapped region (see Fig. 14c), could slightly decrease the values of hardness in that zone denoted by curve C_1 shown in Fig. 13e. In Fig. 14e, a mixture of bainite and carbides is present in the HAZ at location D marked in Fig. 14a, The average hardness of the overlapped region in the HAZ is about 609 HV, and the average hardness in the HAZ of the first track and the second track is 622 and 647 HV, respectively. A drastic variation of hardness is observed below the HAZ in the TZ that affected by the heat. A higher percentage of ferrite and pearlite and a smaller percentage of bainite are present in the TZ marked as E in Fig. 14a, as shown in Fig.14f. The average hardness of the TZ in the first track and the second track is 356 and 377 HV, respectively. The average hardness of the TZ in the overlapped region is about 340 HV.

The prime constituents of BM such as, ferrite and pearlite are present in Fig. 14g, and its hardness is about 210 HV [5]. It is clearly shown in Fig. 14b–d that a higher percentage of martensite is achieved only in the HTZ where a full austenization has occurred. Moreover, the average hardness variation between the overlapped region and the first and second tracks along the cross-section of the heat-treated coupon is about 4.63%. In comparison to other similar works [9, 11, 15, 16], in this study, a minimum hardness variation (4.63%) between the tracks and the overlapped region is achieved. In addition, a fairly even (155~160 μm) depth of heat treatment (see Fig. 14a) is also achieved across the multi-pass heat-treated area. The mean error between the predicted and the measured results is about 2.63%. The minimum error indicates the model can be used to predict the temperature history, phase transformations, and hardness for the MPLHT process.

6 Conclusions

In this study, a 2-kW HPDDL of 808 nm with a uniform distribution (top-hat) of laser power is used to study a MPLHT of the tool steel AISI S7. The heat treatment is performed at various levels of laser power (1,400–1,800 W) and scanning speeds (15–25 mm/s). The tempering effect is studied for different sizes of overlap (1–3 mm) and lengths of scan (10–35 mm). A thermo-kinetic phase transformation model is developed and experimentally verified, that could be used to optimize the heat treatment parameters for the given depth of heat treatment. A good agreement is observed between the thermo-kinetic phase transformation model and experimental ones. The thermo-kinetic phase transformation model results show that the model can be used to predict the temperature history, phase transformations, and hardness for the MPLHT process. The microstructure characterization reveals that a controlled even depth of heat treatment and a uniform hardness distribution can be achieved by using optimal process parameters. A minimum hardness variation and an even depth of heat treatment are achieved for the following processing parameters windows:

- Laser power, 1,400–1,800 W
- Scanning speeds, 15–25 mm/s
- Size of overlap, 3 mm
- Length of scan, 20 mm

Acknowledgments This work was partially supported by NSF Grant # EEC-0541952. The authors greatly acknowledge the help of Andrew Socha, Research Engineer, for the experimental setup, Prabu Balu, PhD candidate for his help in numerical modeling and Dr. Rouzbeh Sarrafi for his valuable comments and review of this work.

References

1. Kathy Kinkade (2006) Diode lasers test their mettle in surface treatment, Laser Focus World: 95–97
2. Safdar S, Li L, Sheikh MA, Liu Z (2006) An analysis of the effect of laser beam geometry on laser transformation hardening. J Manuf Sci Eng 128:659–667
3. Haake JM, Zediker MS (2004) High power direct diode laser successes. SPIE 5336:107–115
4. Kennedy E, Byrne G, Collins DN (2004) A review of the use of high power diode lasers in surface hardening. J Mater Process Technol 155–156:1885–1860
5. Bohler Uddeholm United States (2009) Uddholm Ramax, LH, Stainless Mold Base Steel, www.bucorp.com, Accessed November 2009
6. Foroozmehr E, Kovacevic R (2009) Thermokinetic modeling of phase transformation in the laser powder deposition process. Metall and Mat Trans A 40A:1935–1943
7. Costa L, Vilar R, Reti T, Deus AM (2005) Rapid tooling by laser powder deposition: process simulation using finite element analysis. Acta Mater 53:3987–3999
8. Totten GE, Steel heat treatment handbook: metallurgy and technologies (2006) CRC Taylor & Francis.
9. Lakhar RS, Shin YC, Krane MHM (2008) Predictive modeling of multi-track laser hardening of AISI 4140 steel. Mater Sci Eng, A 480:209–217
10. Yao C, Xu B, Huang J, Zhang P, Wu Y (2010) Study on the softening in overlapping zone by laser-overlapping scanning surface hardening for carbon and alloyed steel. Opt Laser Eng 48:20–26
11. Tani G, Orazi L, Fortunato A, Campana G, Ascari A, Cuccolini G (2008) Optimization strategies of laser hardening of hypo-eutectoid steel, The 41st CIRP Conference on Manufacturing Systems: 355–360.
12. Zhang Z, Delagnes D, Bernhart G (2004) Microstructure evolution of hot-work tool steels during tempering and definition of a kinetic law based on hardness measurements. Mater Sci Eng A 380:222–230
13. Tian Y, Shin YC (2006) Thermal modeling for laser-assisted machining of silicon nitride ceramics with complex features. J Manuf Sci Eng 128:425–434
14. Skvarenina S, Shin YC (2006) Predictive modeling and experimental results for laser hardening of AISI 1536 steel with complex geometric features by a high power diode laser. Surf Coat Technol 201:2256–2269
15. Fortunato A, Orazi L, Tani G (2009) A new computationally efficient model for tempering in multi-tracks laser hardening, Proceedings of the ASME 2009 International Manufacturing Science and Engineering Conference (MSEC 2009) Paper #MSEC2009-84093
16. Campana G, Ascari A, Tani G (2009) A method for laser heat treatment efficiency evaluation in multi-track surface hardening, Proceedings of the ASME 2009 International Manufacturing Science and Engineering Conference (MSEC 2009) Paper #MSEC2009-84095
17. Bailey NS, Shin YC (2009) Optimization of laser hardening processes for industrial parts with complex geometry via predictive modeling, Proceedings of the ASME 2009 International Manufacturing Science and Engineering Conference (MSEC 2009) Paper #MSEC2009-84012
18. Rana J, Goswami GL, Jha SK, Mishra PK, Prasad BVSSS (2007) Experimental studies on the microstructure and hardness of laser-treated steel specimens. Opt Laser Technol 39:385–393
19. Capello E, Previtali B (2008) Optimization of production rate in diode laser hardening. J Laser Appl 20:1–11
20. ANSYS® 11.0 (2009) Manually accessed on November 2009
21. Capello E, Castelnuovo M, Previtali B, Vedani M (2007) Surface treatment of welded duplex stainless steels by diode laser. J Laser Appl 19:133–140
22. Woo HG, Cho HS (1999) Three-dimensional temperature distribution in laser surface hardening processes. IMechE Proc Inst Mech Eng B 213:695–712
23. Kasatkin OG, Vinokur BB, Pilyushenko VL (1984) Calculation models for determining the critical points of steel. Metal Sci Heat Treat 26:27–31
24. Steven W, Haynes AG (1956) The temperature of formation of martensite and bainite in low alloy steels. J Iron Steel Inst 183:349–359
25. Kung CY, Rayment JJ (1982) An examination of the validity of existing empirical formulae for the calculation of M_S temperature. Metall Trans A 13A:328–331
26. Hojerslev C (2001) Tool steels. Riso National Laboratory, Roskilde
27. Kirkaldy JS, Venugopalan D (1983) In: Marder DAR, Goldstein JI (eds) Phase transformations in ferrous alloys. AIME, New York, pp 128–148
28. Li MV, Niebuir DV, Meekiho LL, Atteridge DG (1998) A computational model for the prediction of steel hardenability. Metall and Materi Trans B: 661–672
29. Koistinen DP, Marburger RE (1959) A general equation prescribing the extent of the austenite–martensite transformation in pure iron-carbon alloys and carbon steels. Acta Metall 7:59–60
30. Maynier P, Dollet J, Bastien P (1978) In: Doane DV, Kirkaldy JS (eds) Hardeniability concepts with applications to steels. AIME, New York, pp 163–176
31. Santhanakrishnan S, Kong F, Kovacevic R (2009) A three-dimensional transient modeling and experimental analysis of laser transformation hardening by using high power direct diode laser, Proceedings of the ASME 2009 International Manufacturing Science and Engineering Conference (MSEC 2009) Paper #MSEC2009-84152